nature nanotechnology

ARTICLES

https://doi.org/10.1038/s41565-020-0670-0

Probing nanoscale fluctuation of ferromagnetic meta-atoms with a stochastic photonic spin Hall effect

Bo Wang, Kexiu Rong, Elhanan Maguid, Vladimir Kleiner and Erez Hasman ✉

The photonic spin Hall effect, a deep subdiffraction-limited shift between the opposite spin components of light, emerges when light undergoes an evolution of polarization or trajectory that induces the geometric phase. Here, we study a stochastic photonic spin Hall effect arising from space-variant Berry–Zak phases, which are generated by disordered magneto-optical effects. This spin shift is observed from a spatially bounded lattice of ferromagnetic meta-atoms displaying nanoscale disorders. A random variation of the radii of the meta-atoms induces the nanoscale fluctuation. The standard deviation of the probability distribution of the spin shifts is proportional to the fluctuation of the meta-atoms. This enables us to detect a five-nanometre fluctuation by measuring the probability distribution of the spin shifts via weak measurements. Our approach may be used for sensing deep-subwavelength disorders by actively breaking the photonic spin symmetry and may enable investigations of fluctuation effects in magnetic nanosystems.

The study of the interaction of light with disordered nanostructures has offered us a wealth of interesting effects and numerous potential applications[1–3]. One kind of disorder-based application is to overcome the undesirable optical scattering from strong disorders (a wavelength-scale or larger inhomogeneity)[4] and enable highly efficient light manipulations, such as optimal photonic transport[5,6], subwavelength focusing[7] and wavefront shaping[8]. Moreover, optical metrologies that can measure extremely weak disorders at the deep-subwavelength scale play a crucial role in extreme nanophotonic and electronic applications. Very recently, growing attention has been paid to this field, yielding photonic applications for extreme subwavelength sensing that approaches the atomic scale[9,10].

A challenge of dealing with weakly disordered nanostructures is the limited opportunities to extract the information from subtle light–matter interactions. The stochastic nature and negligible spatial fluctuation of disordered nanostructures serve as a barrier that hinders light from detecting any useful information other than that from a homogeneous material. This problem can be approached by seeking special optical conditions such as the critical angle[9], broken symmetry[11] or resonant effects[12]. The resonant nature of a nanoantenna affords substantial control over the local scattering of light by tailoring the nanoantenna size and shape[13–18]. Moreover, anisotropic nanoantennas can introduce polarization-dependent phenomena due to the breaking of the structural symmetry. An array of anisotropic nanoantennas with random in-plane orientations gives rise to photonic spin-dependent effects[11]. These phenomena arise from a disordered Pancharatnam–Berry phase (geometric phase), which provides a photonic spin–orbit interaction mechanism[19–22]. However, the spin-dependent effects will naturally disappear if the anisotropic nanoantennas are replaced by isotropic ones, for example, circular nanoantennas.

A magnetic field can tailor light–matter interactions by controlling light on its spin basis, without the requirement for any breaking of the structural symmetry. This is achieved by changing the optical properties of the materials via magnetization (M). Homogeneously magnetized media give rise to magneto-optical effects, such as Faraday and Kerr effects that manipulate the polarization states of light. These effects not only serve as powerful tools for investigating topological and quantum phenomena in solid-state physics[23] but also offer numerous optics applications, such as isolators, storage units and many others[24,25]. When light encounters inhomogeneously magnetized media, a distinct phenomenon emerges: light bends its trajectory, resembling a photonic Hall effect[26]. Likewise, when an electron travels through inhomogeneous magnetizations, its trajectory deflects. This electronic phenomenon is known as the topological Hall effect if the inhomogeneity of the magnetization is confined to the nanoscale, forming a magnetic topological defect[27]. The photonic spin Hall effect (PSHE), an analogue of the solid-state spin Hall effect, was extensively studied in non-magnetic systems[28–32]. The spin-split modes in the curved or broken trajectories of light originate from the geometric phases between different plane-wave components with distinct wave vectors, that is, the 'spin redirection' geometric phases[30,31,33,34].

In this article, we experimentally detected nanoscale fluctuations of isotropic nanoantennas by a stochastic PSHE induced by the Berry–Zak phase. The spatial fluctuation is implemented via the differentiation of meta-atoms, that is, by randomly varying the radii of circular ferromagnetic nanoantennas arranged in a lattice with a subwavelength period (Fig. 1). A moderate external magnetic field is employed to magnetize the lattice. On this spin basis, discriminations of the scattering phases between spin-up ($|\sigma_+\rangle$) and spin-down ($|\sigma_-\rangle$) states emerge upon the meta-atoms, manifesting as magnetization-induced geometric phases, that is, the Berry–Zak phases[19,20,35]. The disordered Berry–Zak phases give rise to a spin-dependent shift of light in the momentum space, which varies for different realizations of the disorders. In this work, a typical shift between opposite spin components (that is, the spin shift) is five orders of magnitude smaller than the diffraction-limited spot, which is observed via a weak measurement[33,36]. Statistically, the value of the

Micro and Nanooptics Laboratory, Faculty of Mechanical Engineering and Russell Berrie Nanotechnology Institute, Technion, Israel Institute of Technology, Haifa, Israel. ✉e-mail: mehasman@technion.ac.il

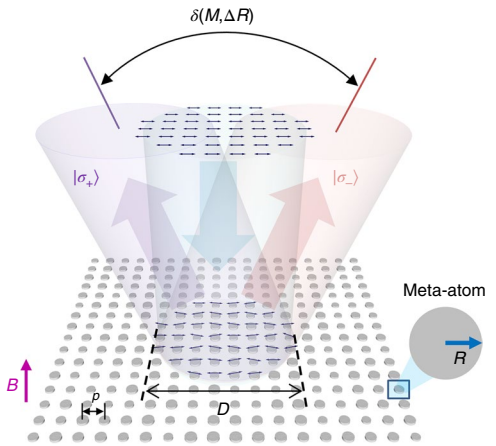

Fig. 1 | Conceptual illustration of a PSHE from a disordered ferromagnetic metasurface. The metasurface consists of a square array of circular nickel nanoantennas, that is, the meta-atoms. The period of the array (p) is on a subwavelength scale. The radii of meta-atoms (R) are spatially fluctuated in the range of ΔR. An external magnetic field (B) along the normal direction is employed to magnetize the metasurface. A linearly polarized beam with a diameter D impinges onto the disordered ferromagnetic metasurface at a normal angle (indicated by the central arrow). The incident polarization of the beam is indicated by the array of aligned line segments with blue arrowheads. Due to the fluctuation of magneto-optical effects associated with the random sizes of the meta-atoms, the reflected light from the metasurface possesses space-variant polarizations, which emerge above the meta-atoms in the near field; these polarizations are indicated by an array of randomly orientated line segments with arrowheads. In the momentum space, spin-dependent diffraction-limited spots split (exaggerated in the sketch) at a distance of δ, depending on ΔR and the normalized magnetization $M \in [-1,1]$.

spin shift obeys a Gaussian probability distribution, the standard deviation of which is related to the fluctuation of the radii of the meta-atoms. We demonstrated the detection of a five-nanometre fluctuation of the meta-atoms from the measured statistical distribution of the PSHEs. The incorporation of magneto-optical effects and nanophotonics provides an active means for the space-variant modulation of light, which offers exciting opportunities to engineer the light–matter interaction at the nanoscale.

PSHE arising from disordered Berry–Zak phases

Magneto-optical Kerr rotation (θ_K) describes the polarization rotation of a linearly polarized light reflecting from a magnetized material. In general, Kerr rotations from smooth thin films of ferromagnetic metals are very weak, because of the limited length of light–matter interactions. However, metallic nanostructures can substantially enhance the effects by exploiting plasmonic resonance due to the increased Lorentz force from the collective movement of the electrons[37–39]. Considering a square lattice (period of $p = 400$ nm) composed of circular nickel nanoantennas with a uniform radius R and a height $h = 170$ nm, the Kerr rotation at the wavelength $\lambda = 632.8$ nm changes as a function of R, as shown in Fig. 2a. Here, an enhancement of θ_K arises around $R = 125$ nm, where the resonant effect emerges (Supplementary Section 1). For nanoantennas farther away from the resonant region, the Kerr rotation decreases substantially. Therefore, the sensitive Kerr rotation around the resonant region can be utilized to detect the size changes of the array of uniform nanoantennas.

Instead of dealing with a lattice of nanoantennas with identical size, here, we are interested in a different situation, where there is a size fluctuation of the nanoantennas. To realize this disordered system, we design a metasurface constructed from an array of circular nickel nanoantennas (that is, meta-atoms) in a subwavelength period. The spatial fluctuation is introduced by randomly varying the radii of the meta-atoms on the scale of a few nanometres (Fig. 1). In general, the radii of the meta-atoms in a disordered metasurface can be expressed as $R(x,y) = R_0 + \Delta R \times f(x,y)$. Here, (x,y) are the locations of the meta-atoms, R_0 is the average radius, ΔR is the fluctuation range of $R(x,y)$ and $f(x,y) \in [-1,1]$ is a two-dimensional (2D) random function with a flat probability distribution (Supplementary Fig. 2). Initially, a one-dimensional (1D) disordered metasurface is considered, where the radii of the meta-atoms are described as $R(x) = R_0 + \Delta R \times f(x)$. An example of $R(x)$ is shown in Fig. 2b (upper panel), where we set $R_0 = 115$ nm and $\Delta R = 5$ nm. R_0 is located in the resonant region with large $\partial\theta_K/\partial R$; hence, $R(x)$ reaches a large fluctuation range of the Kerr rotations ($\Delta\theta_{K1}$; Fig. 2a). Before being magnetized (when $M = 0$), the metasurface has a typical isotropic configuration without any polarization manipulations. Note that in general M is nonzero for the nickel meta-atoms even without an external magnetic field[40]; however, to simplify the analysis, we neglect this effect since it is weak compared with the phenomenon we study. The spatial fluctuation of the meta-atoms induces small and random polarization-independent resonant phases $\phi_0(x)$ in the reflection coefficient (Fig. 2b, middle panel and Supplementary Section 1). As calculated using a Fourier transform, $\phi_0(x)$ gives rise to a spin-independent diffraction-limited spot I_0 in the momentum space, with $S_3 = 0$ (Fig. 2d, left panel); here, $S_3 = (I_{\sigma+} - I_{\sigma-})/(I_{\sigma+} + I_{\sigma-})$ is the third Stokes parameter, and $I_{\sigma\pm}$ denotes the normalized intensity distributions in the momentum space for $|\sigma_\pm\rangle$. Additionally, we find that the centre of I_0, that is, $\delta_0 = \langle k_x \rangle = \int k_x I_0 \mathrm{d}^2k / \int I_0 \mathrm{d}^2k$, is slightly shifted from that ($\delta_0 = 0$) of a reference metasurface with $\Delta R = 0$ (Supplementary Section 1). Here, $\mathrm{d}^2k = \mathrm{d}k_x\mathrm{d}k_y$, and δ_0 is $\sim 10^{-2}(\lambda/D)$; (k_x,k_y) denotes the momentum space normalized by $k_l = 2\pi/\lambda$; D is the diameter of a beam impinged onto the metasurface; and λ/D is the diffraction limit. The shift δ_0 originates from the spatially bounded disordered metasurface for $M = 0$. Since there is no symmetry breaking yet, the spin components are degenerated.

Once the metasurface is magnetized (for example, $M = 1$), space-variant Kerr rotations $\theta_K(x)$ will emerge due to the distinct local magneto-optical responses associated with different sizes of the meta-atoms. Considering two meta-atoms of radii R_1 and R_2 in the metasurface (Fig. 2b, upper panel), the polarizations of the incident (black dot) and reflected (coloured dots) light are presented by different points on the equator of the Poincare sphere (Fig. 2c, right panel). By projecting the two polarizations to $|\sigma_+\rangle$ via different geodesic paths, a nonzero solid angle Ω forms, indicating a geometric phase difference $\phi_g = \sigma_+\Omega/2$ between the two meta-atoms[21]. Similarly, a geometric phase difference $\phi_g = \sigma_-\Omega/2$ applies for the projection to $|\sigma_-\rangle$; here, $\Omega = 2\mathrm{d}\theta_K$, $\sigma_\pm = \pm 1$ and $\mathrm{d}\theta_K$ is the difference in the Kerr rotations between the two meta-atoms. In general, the spatial fluctuation of Kerr rotations gives rise to space-variant geometric phases, which relate to the local Kerr rotations by $\phi_g(x) = \sigma_\pm\theta_K(x)$ (Supplementary Section 1). We refer to this geometric phase as a Berry–Zak phase[35]. The total phase pickups of the reflected light are composed of both the resonant phases and the spin-dependent Berry–Zak phases, that is, $\phi(x) = \phi_0(x) + \phi_g(x)$. By calculating the momentum space from $\phi(x)$ using a Fourier transform (Supplementary Section 1), we obtain a pair of spin-dependent diffraction-limited spots $I_{\sigma\pm}$ that are shifted away from each other. The spin shifts in the x and y directions are defined as $\delta_i = \int k_i I_{\sigma_+} \mathrm{d}^2k / \int I_{\sigma_+} \mathrm{d}^2k - \int k_i I_{\sigma_-} \mathrm{d}^2k / \int I_{\sigma_-} \mathrm{d}^2k$, with $i = x,y$. For the 1D disordered case, we obtain $\delta_y = 0$, while δ_x is approximately four orders of magnitude smaller than the diffraction-limited spot (Fig. 2d, right panel). The spin shift δ_x is the PSHE induced by the disordered Kerr rotations, that is, $\Delta\theta_{K1}$, depending on ΔR and M. Moreover, δ_x denotes the difference of the eigenvalues between

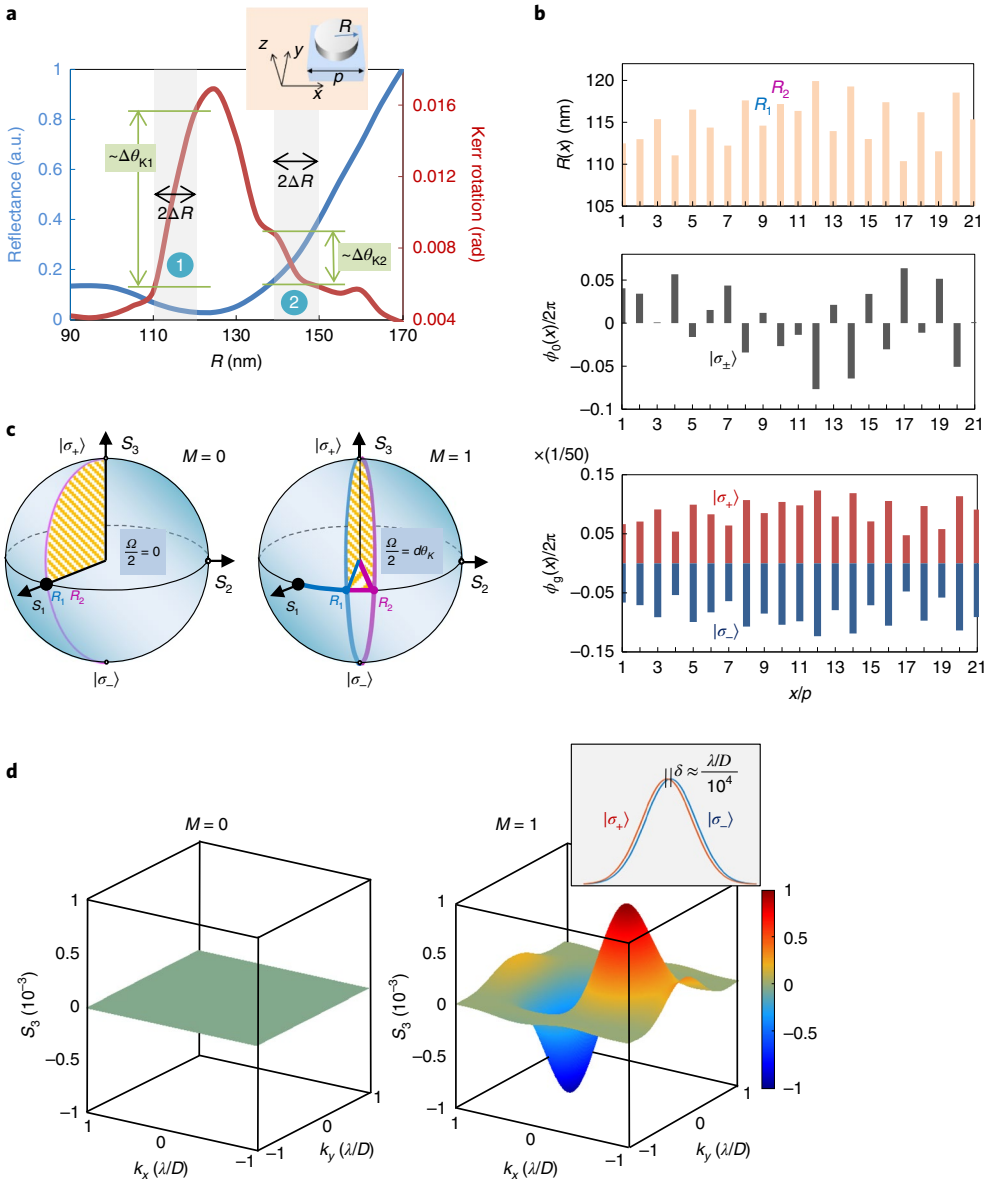

Fig. 2 | The Kerr rotation, Berry–Zak phase and PSHE from a disordered ferromagnetic metasurface. a, The calculated Kerr rotation θ_K and reflection as a function of the radius R of circular nickel nanoantennas in a periodic lattice. The peak of the Kerr rotation and the valley of reflection indicate a resonant effect at approximately $R = 125$ nm. In the simulation, x-polarized light at a wavelength of 632.8 nm impinges onto the periodic structure ($p = 400$ nm) at a normal angle. Only one unit of the structure (the inset; see also Supplementary Fig. 1) is utilized in the simulation by applying periodic boundary conditions. The refractive indices of the nickel nanoantennas and the silica substrate are $n_{nickel} = 1.9-4i$ and $n_{silica} = 1.45$, respectively. The magneto-optical parameter is set as $Q = (8.5 + 6.5i) \times 10^{-3}$, and the magnetization is set as $M = 1$, with the magnetic field B along the z direction. The left shaded area (region 1) is located in the resonant region, spanning a large range of Kerr rotations, $\Delta\theta_{K1}$. The right area (region 2) is far away from the resonant region, spanning a smaller range of Kerr rotations, $\Delta\theta_{K2}$. **b**, The calculated resonant phases $\phi_0(x)$ and geometric phases $\phi_g(x)$ of an example 1D disordered metasurface with a radius distribution $R(x)$ for the meta-atoms. On the bottom plot, x(1/50) denotes that the value range of the y axis is [−0.15, 0.15] x(1/50). **c**, The magnetization-induced geometric phase interpreted on the Poincare spheres using two meta-atoms with radii R_1 and R_2 (shown in **b**). The left and right panels show the cases before and after the metasurface is magnetized, respectively. **d**, The S_3 distributions in the momentum space before (left) and after (right) the magnetization. Inset: exaggerated illustration of the spin shift of light.

the eigenstates, $|\sigma_\pm\rangle$, of the photon's spin operator that coupled to the position of the beam in the momentum space. It is possible to amplify the difference by projecting the spin states into different superposition states using the weak measurement[36].

Observation of PSHE from spatial nanoscale fluctuations

The experimental observation of the PSHE via a weak measurement can be achieved by applying a preselection polarization and a postselection polarization that are nearly orthogonal to each other, as shown in Fig. 3a. The observed spot in the momentum space, I_β, varies with the orientation β of the postselection polarizer. The centroids of the spot, defined as $\langle k_i \rangle_\beta = \int k_i I_\beta \mathrm{d}^2k / \int I_\beta \mathrm{d}^2k$, give the amplified spin shifts by $A_\beta \delta_i = \langle k_i \rangle_\beta - \langle k_i \rangle_{-\beta}$, with A_β being the amplification factor (Supplementary Section 2).

To demonstrate the PSHE that arises purely from the spatial fluctuation of the meta-atoms, we fabricated a 1D disordered

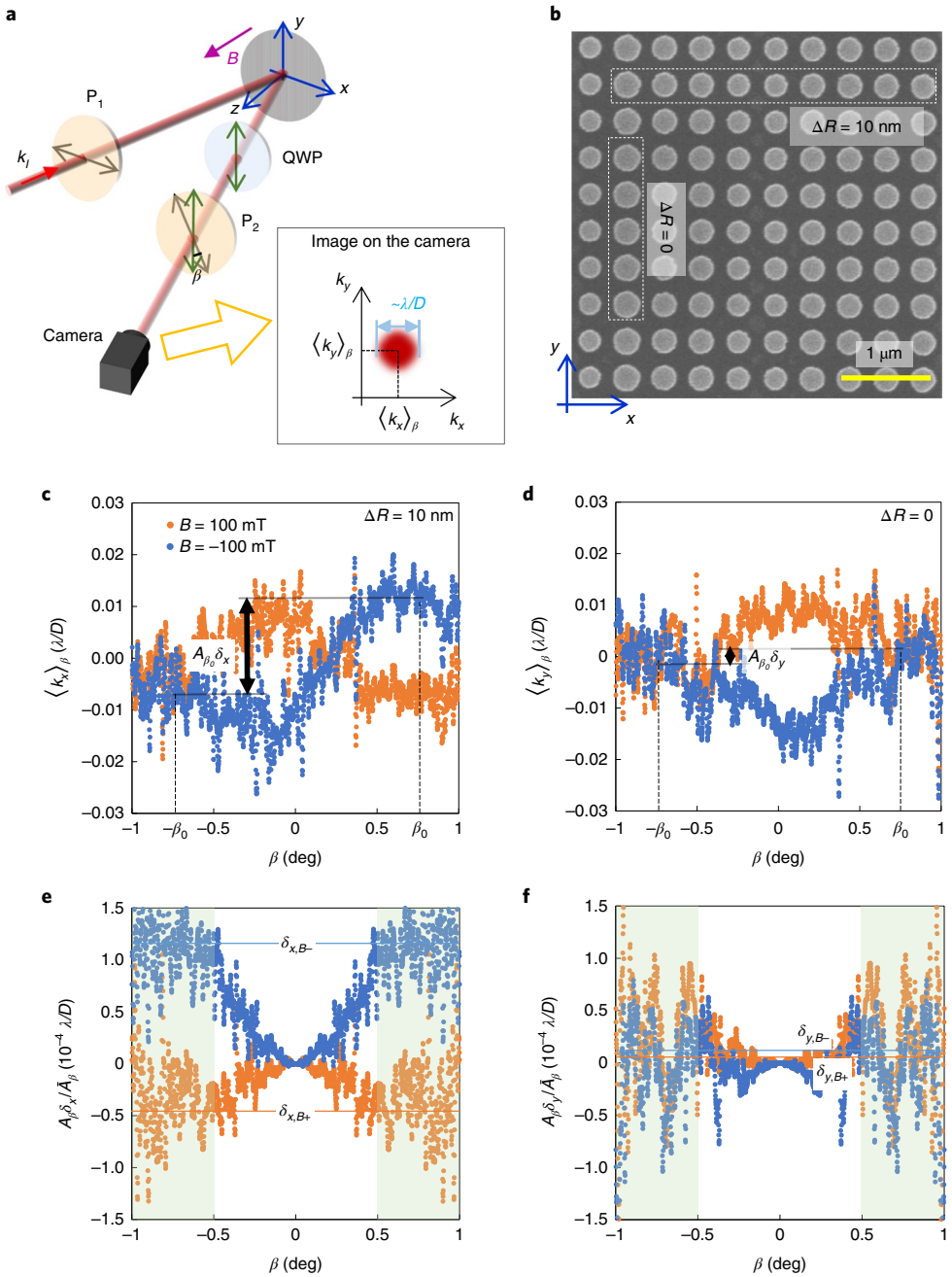

Fig. 3 | Observation of the PSHE from the nanoscale fluctuation of ferromagnetic meta-atoms. a, The schematic experimental setup for the weak measurement. P_1 and P_2 denote polarizers (transmission axes marked with arrows), and QWP denotes a quarter-wave plate (fast axis marked with an arrow). The symbol β indicates the orientation of P_2, and $\beta = 0$ denotes the orthogonal polarization between P_1 and P_2. The charge-coupled device (CCD) camera is used to capture the image of the beam in the momentum space (the lens system is not shown). The centres of the spot, namely, $\langle k_x \rangle_\beta$ and $\langle k_y \rangle_\beta$, change as a function of β, and are evaluated by integrating the intensity distribution of the beam over the momentum space. **b**, Scanning electron microscopy (SEM) image of the 1D disordered metasurface. The nanoscale fluctuation of the radii of meta-atoms is introduced along the x axis. **c**,**d**, The measured $\langle k_i \rangle_\beta$ as a function of β in the x (**c**) and y (**d**) directions. Here, $\beta_0 = 0.75°$ is chosen to illustrate the amplified spin shifts, $A_{\beta_0}\delta_i$. The vertical lines with arrowheads show the amplified spin shifts in each direction. **e**,**f**, The measured $A_\beta \delta_i / \bar{A}_\beta$ as a function of β in the x (**e**) and y (**f**) directions. Here, $A_\beta \delta_i$ in **e** and **f** are the experimental results of $\langle k_i \rangle_\beta - \langle k_i \rangle_{-\beta}$ calculated from **c** and **d**, respectively. The shaded areas in **e** are the valid regions for the approximation $A_\beta \approx \bar{A}_\beta$, with $\beta_C \approx 0.5°$ being the critical angle. The blue and orange horizontal lines in **e** denote the saturated values of $A_\beta \delta_x / \bar{A}_\beta$, indicating the spin shifts $\delta_{x,B\pm}$. The blue and orange horizontal lines in **f** show the evaluated system noise.

metasurface. The average radius of the meta-atoms R_0 was 115 nm, which was in the calculated resonant region (Fig. 2a), and the range of the radius fluctuation ΔR was 10 nm. The disorder was introduced along the x direction, and for comparison, there was no disorder along the y direction (Fig. 3b). We used a He–Ne laser ($\lambda = 632.8$ nm, spot diameter $D = 80$ μm) to illuminate the metasurface (size of 200 μm) at a small incident angle (~10°) to avoid unwanted multiple reflections (Fig. 3a). The background effect of

the off-axis illumination was measured for zero magnetic field, which was subtracted from the measured $\langle k_i\rangle_\beta$ at a magnetic field of $B=\pm100$ mT (Supplementary Section 2).

The measured curves of $\langle k_i\rangle_\beta$ are shown in Fig. 3c,d, where distinct behaviours are observed in the x and y directions. In the y direction (Fig. 3d) without the fluctuation of the meta-atoms, a symmetric behaviour of $\langle k_y\rangle_\beta$, that is, $\langle k_y\rangle_\beta \approx \langle k_y\rangle_{-\beta}$, is obtained. This property indicates negligible PSHEs, as the amplified spin shifts $A_\beta\delta_y=\langle k_y\rangle_\beta-\langle k_y\rangle_{-\beta}\approx 0$. The nonvanishing $\langle k_y\rangle_\beta$ values in the vicinity of $\beta=0$ are not indications of PSHE. Rather, they are the deflections of the cross-polarized light, which is generated from homogeneous magnetization (Supplementary Fig. 5). By contrast, in the x direction with the spatial fluctuation (Fig. 3c), we observe an anti-symmetric behaviour of $\langle k_x\rangle_\beta$, that is, $\langle k_x\rangle_\beta \approx -\langle k_x\rangle_{-\beta}$. Obviously, $A_\beta\delta_x=\langle k_x\rangle_\beta-\langle k_x\rangle_{-\beta}\neq 0$, and a PSHE emerges.

The value of the spin shift in the experiment can be calculated from A_β. Generally, A_β is complicated, but it approximates a simple function of β, that is, $A_\beta = 2/\tan(\beta)$, when the absolute value of β is larger than a critical angle β_C (that is, $|\beta|>|\beta_C|$; Supplementary Fig. 6). By evaluating the curve of $A_\beta\delta_i/\bar{A}_\beta$, we can obtain both β_C and the spin shift δ_i. This is because $A_\beta\delta_i/\bar{A}_\beta \approx \delta_i$ when $|\beta|>|\beta_C|$. The measured curves of $A_\beta\delta_i/\bar{A}_\beta$ are shown in Fig. 3e,f. Here, $A_\beta\delta_i$ values are calculated from the measured results of $\langle k_i\rangle_\beta-\langle k_i\rangle_{-\beta}$ in Fig. 3c,d. In the x direction, $A_\beta\delta_x/\bar{A}_\beta$ increases with small β, and it is saturated for $\beta\geq 0.5°$. This means that, in this experiment, $\beta_C\approx 0.5°$, and the spin shift can be evaluated from the saturated value of $A_\beta\delta_x/\bar{A}_\beta$ for $\beta>0.5°$. The obtained spin shifts are $\delta_{x,B-}=1.1\times10^{-4}(\lambda/D)$ and $\delta_{x,B+}=-4.1\times10^{-5}(\lambda/D)$ for opposite magnetic fields $B=-100$ mT and $B=+100$ mT, respectively. Ideally, we should have $\delta_{x,B-}=-\delta_{x,B+}$. The discrepancy is caused by the system noise and the hysteresis of the PSHE from the ferromagnetic meta-atoms (Supplementary Fig. 7). In the y direction, the curves for $A_\beta\delta_y/\bar{A}_\beta$ oscillate strongly with β, without any saturated value. Nevertheless, we can still evaluate the spin shifts characterizing the noise level of the measurements $\delta_{y,B+}=1.9\times10^{-6}(\lambda/D)$ and $\delta_{y,B-}=6.3\times10^{-6}(\lambda/D)$, which are much smaller than the PSHEs observed in the x direction.

The stochastic behaviour of the PSHE

The PSHE is observed from a spatially bounded disordered system; the area for light–matter interaction is limited. For different realizations of the disorder, distinct spin shifts are obtained in the calculation (Supplementary Fig. 3), indicating a stochastic behaviour of the effect. As previously reported, spatially bounded disorders have shown many interesting phenomena. For instance, a compositionally disordered structure can be utilized to tailor the band-tail modes (Anderson localization modes in the bandgap) in random lasers[41]. In addition, superoscillatory fields (subwavelength-scale features of waves) can also be realized from a disordered system, enabling super-resolution imaging in optics[36,42,43].

For a stochastic phenomenon, it is important to evaluate the probability distribution of the effects over many different disorders. This can be achieved by repeating the calculation many times under the same conditions (D, ΔR, R_0, M and so on), each time with a different realization of disorder (Supplementary Section 5). By evaluating the PSHEs from a large number (10^4) of 1D disordered metasurfaces with different random functions $f(x)$, we observe a Gaussian probability distribution for the spin shifts, that is, $P(\delta_x) = \left(1/\Delta\delta_{1D}\sqrt{2\pi}\right)\exp\left(-\delta_x^2/2\Delta\delta_{1D}^2\right)$, with $\Delta\delta_{1D}$ being the standard deviation (Fig. 4b and Supplementary Section 5). It is worth noting that for each metasurface, there is a linear correlation between the spin shift δ_x and the average of the local geometric phase gradients $\langle\partial\phi_g/\partial x\rangle$ (Supplementary Fig. 9). By statistically exploring this relation, we obtain the standard deviation $\Delta\delta_{1D}$ as proportional to $\Delta\phi_g/D$, with $\Delta\phi_g$ being the fluctuation range of the Berry–Zak phases (Supplementary Section 5). Note that the Berry–Zak phase is proportional to the magnetization M and the radius $R(x)$ of the meta-atoms, which are located in the resonant region with a small ΔR (Fig. 2a, $\Delta R<10$ nm). Therefore, the $\Delta\delta_{1D}$ approximately obeys a simple relation of $\Delta\delta_{1D}$ being proportional to $M\Delta R/D$. If M or ΔR is zero, the spatial fluctuation of the Berry–Zak phases ($M\Delta R$) disappears. As a result, the Gaussian distribution becomes a delta function, and the probability of observing the PSHE vanishes. Similarly, the spin shift also disappears for an infinite system, as $\Delta\delta_{1D}\propto 1/D\rightarrow 0$ for $D\rightarrow\infty$ (Fig. 4b, inset), revealing the behaviour of the PSHE in a spatially bounded system. Moreover, we also evaluated the PSHEs from numerous 2D disordered metasurfaces with different realizations of $f(x,y)$ and obtained a 2D Gaussian distribution $P(\delta_x,\delta_y)$, as shown in Fig. 4f. In addition, we found that the standard deviations of the distributions are very different between the 1D and 2D cases for the same ΔR (Fig. 4b,c). By comparison, only the spin shifts in the x direction are considered. The corresponding probability distribution for the 2D case is $P(\delta_x)=\int P(\delta_x,\delta_y)\mathrm{d}\delta_y = \left(1/\Delta\delta_{2D}\sqrt{2\pi}\right)\exp\left(-\delta_x^2/2\Delta\delta_{2D}^2\right)$, with $\Delta\delta_{2D}$ being the standard deviation. As shown in Fig. 4b,c, $\Delta\delta_{1D}\gg\Delta\delta_{2D}$. Moreover, by keeping a constant D in the statistical calculation while changing the density of the meta-atoms, a ratio of $\Delta\delta_{1D}/\Delta\delta_{2D}=\sqrt{N}$ is obtained (the inset of Fig. 4c), where N is the number of meta-atoms in D.

Experimentally, we fabricated a series of large disordered metasurfaces, each with a size of 200 μm × 1,000 μm. For statistical measurements, the beam with a diameter $D\approx 80$ μm impinges onto every metasurface multiple times (~30), each time at a different location (by moving the beam for ~30 μm per step along the longer side of the large metasurface) to achieve distinct realizations of random function (Fig. 4a). The measured PSHEs from the 1D and 2D disordered metasurfaces with the same $\Delta R=20$ nm are presented in Fig. 4d,e, where the statistical distributions demonstrate the stochastic behaviour of the PSHE. Moreover, the standard deviation of the distribution in the 1D case is larger than that in the 2D case, indicating the strong dependence of the effects on the disorder dimensionalities, which is in agreement with our prediction. Note that the observed standard deviation for 2D disordered metasurfaces is larger than the theoretical expectation, as the small spin shifts approach the noise level of our measurement.

To demonstrate the relation between the nanoscale spatial fluctuation ΔR and the probability distribution of the PSHEs, we also fabricated 1D disordered metasurfaces with $\Delta R=5$ nm, 10 nm and 20 nm. Similarly, multiple measurements (~30) were conducted for each metasurface to obtain the distributions of the PSHEs and evaluate the corresponding standard deviations. The measured $\Delta\delta_{1D}$ for different ΔR values is shown in Fig. 4g, in good agreement with the theoretical curve calculated from numerous disordered metasurfaces (Supplementary Section 5). For ΔR smaller than ~10 nm, $\Delta\delta_{1D}$ increases linearly with ΔR, as predicted by our theoretical analysis (Fig. 2a, region 1). The width of the linear region (the orange area in Fig. 4g) agrees with that of the resonant region for the Kerr rotations (Fig. 2a). For $\Delta R\approx 10$ nm, the spatial fluctuation of the Kerr rotations reaches a maximum. Further increasing ΔR does not yield stronger fluctuation of the Kerr rotations or Berry–Zak phases; hence, the standard deviation saturates.

Conclusions

We demonstrate an optical approach to detect extremely weak radius fluctuation of meta-atoms in a lattice by measuring the probability distribution of the PSHEs. This sensitive effect can be extended to different types of geometric disorders and is potentially applicable in detecting nanoscale fabrication errors for on-chip nanodevices. Although we used a ferromagnetic material to demonstrate this effect, it is also possible to observe the PSHE from disordered nanostructures made of other materials, such as gold[38], with moderate

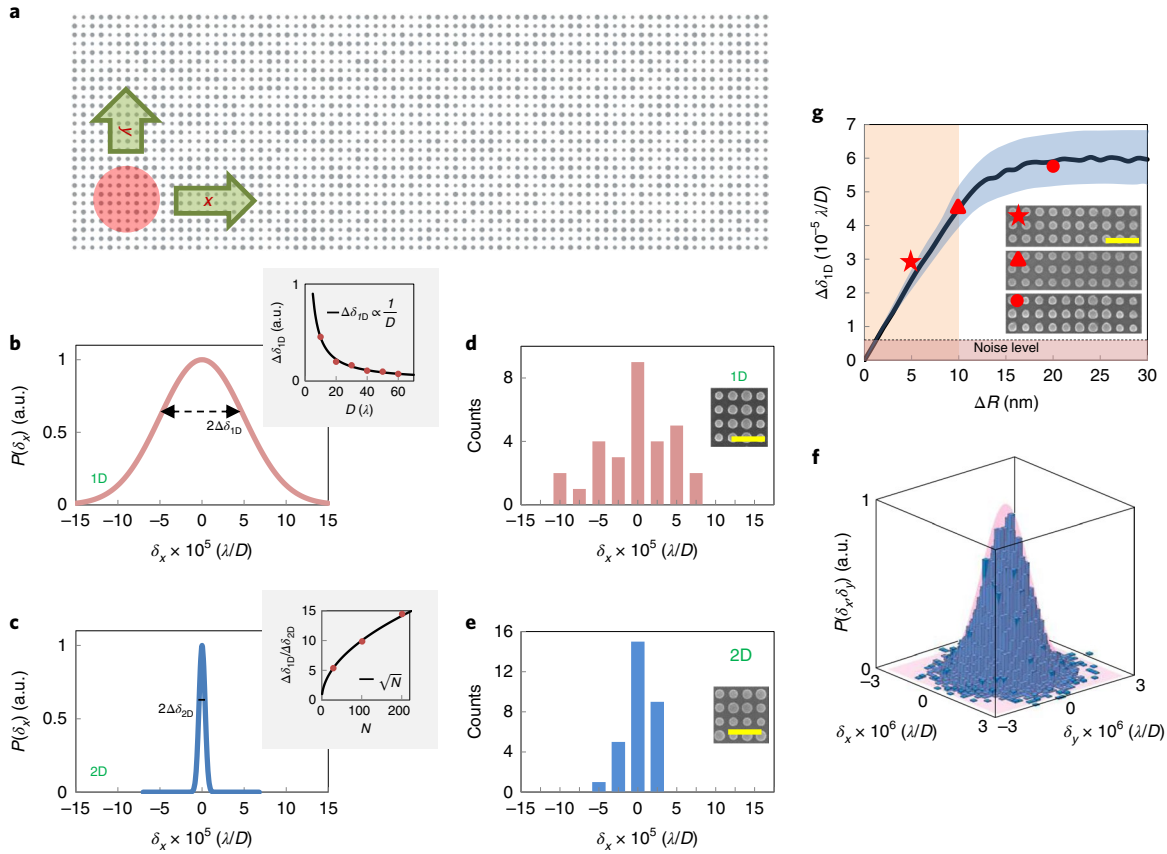

Fig. 4 | The stochastic properties of PSHEs from disordered metasurfaces. a, Illustration of the statistical approach in the experiments. Different realizations of the random functions are achieved by scanning the beam (the red circle) across the metasurface along x and y directions (the arrows). At each location, the weak measurements are carried out by taking $\beta = \pm 1°$, corresponding to an amplification factor $A_{|\beta|} \approx 114.6$. The spin shift is evaluated by $\delta_x = (\delta_{x,B+} - \delta_{x,B-})/2$, via applying opposite magnetic fields $B = \pm 100$ mT. **b**,**c**, The fitted Gaussian probability distributions $P(\delta_x)$ of the PSHE for 1D (**b**) and 2D (**c**) disordered metasurfaces. The inset of **b** depicts the calculated standard deviation ($\Delta\delta_{1D}$) of the PSHE as a function of D (in the unit of wavelength λ). The calculation results (dots) obey the relation $1/D$ (the curve), with a constant fitting parameter. The inset of **c** depicts the ratio of the standard deviations of the PSHE between the 1D and 2D cases as a function of N, the number of meta-atoms across D. The curve depicts the theoretic values $\sqrt{N}$, and the dots are the calculated results. Every point in the insets of **b** and **c** is calculated from numerous (>10^4) disordered metasurfaces. **d**,**e**, The measured distributions of the PSHEs for 1D (**d**) and 2D (**e**) disordered metasurfaces. The insets are the SEM images. **f**, The calculated $P(\delta_x,\delta_y)$ for 2D disordered metasurfaces. The pillars are the calculations, and the pink surface is the fitted Gaussian distribution. **g**, The experimental results (red marks) of the standard deviation of PSHEs as a function of the spatial fluctuation ΔR. The black curve is the calculated $\Delta\delta_{1D}$ from numerous (10^4) disorders, and the blue area denotes the standard deviation of the estimated $\Delta\delta_{1D}$ from 30 disorders. The half width of the blue area is approximately 13% of $\Delta\delta_{1D}$ (Supplementary Fig. 10). The orange area denotes the region where $\Delta\delta_{1D}$ increases linearly with ΔR. The pink area denotes the detection limit of our system, that is, the noise level. Insets depict the SEM images of metasurfaces with different ΔR. All the scale bars are 1 μm.

magnetic fields. Essentially, the spin shifts arise from space-variant Berry–Zak phases, which are induced by magneto-optical effects in the spatially bounded disordered systems. Alternatively, these magneto-optical effects can be achieved due to spatial fluctuation of the magnetization or the magnetic field, such as the disordered magnetism in 2D materials[44,45], the frustrated magnetism in artificial spin ices[46–49] or the magnetic field fluctuation of the vacuum state[50], which can inspire further explorations of these effects via PSHE. The combination of the spatially bounded resonant phase and Berry–Zak phase provides opportunities for controlling disordered nanophotonics such as the Anderson localization modes and superoscillation using a magnetic field. The Berry–Zak phase can be utilized to develop reconfigurable nanophotonic devices via customized magnetizations. Enhanced magnetizations may even lead towards active metasurfaces for dynamic wavefront shaping. Moreover, the PSHE can also be induced from magnetic-controlled nanoscale topological defects, enabling the detection of topological nanostructures (Supplementary Fig. 8).

Online content

Any methods, additional references, Nature Research reporting summaries, source data, extended data, supplementary information, acknowledgements, peer review information; details of author contributions and competing interests; and statements of data and code availability are available at https://doi.org/10.1038/s41565-020-0670-0.

Received: 10 October 2019; Accepted: 9 March 2020;
Published online: 27 April 2020

References

1. Wiersma, D. S. Disordered photonics. *Nat. Photon.* **7**, 188–196 (2013).
2. Segev, M., Silberberg, Y. & Christodoulides, D. N. Anderson localization of light. *Nat. Photon.* **7**, 197–204 (2013).
3. Stockman, M. I. Inhomogeneous eigenmode localization, chaos, and correlations in large disordered clusters. *Phys. Rev. E* **56**, 6494–6507 (1997).

4. Vellekoop, I. M. & Mosk, A. P. Focusing coherent light through opaque strongly scattering media. *Opt. Lett.* **32**, 2309–2311 (2007).
5. Kim, M. et al. Maximal energy transport through disordered media with the implementation of transmission eigenchannels. *Nat. Photon.* **6**, 581–585 (2012).
6. Levi, L. et al. Disorder-enhanced transport in photonic quasicrystals. *Science* **332**, 1541–1544 (2011).
7. Park, J. H. et al. Subwavelength light focusing using random nanoparticles. *Nat. Photon.* **7**, 454–458 (2013).
8. Jang, M. et al. Wavefront shaping with disorder-engineered metasurfaces. *Nat. Photon.* **12**, 84–90 (2018).
9. Sheinfux, H. H. et al. Observation of Anderson localization in disordered nanophotonic structures. *Science* **356**, 953–956 (2017).
10. Yuan, G. & Zheludev, N. I. Detecting nanometric displacements with optical ruler metrology. *Science* **364**, 771–775 (2019).
11. Maguid, E. et al. Disorder-induced optical transition from spin Hall to random Rashba effect. *Science* **358**, 1411–1415 (2017).
12. Pors, A., Ding, F., Chen, Y., Radko, I. P. & Bozhevolnyi, S. I. Random-phase metasurfaces at optical wavelengths. *Sci. Rep.* **6**, 28448 (2016).
13. Kildishev, A. V., Boltasseva, A. & Shalaev, V. M. Planar photonics with metasurfaces. *Science* **339**, 1232009 (2013).
14. Minovich, A. E. et al. Functional and nonlinear optical metasurfaces. *Laser Photonics Rev.* **9**, 195–213 (2015).
15. Wang, Q. et al. Optically reconfigurable metasurfaces and photonic devices based on phase change materials. *Nat. Photon.* **10**, 60–65 (2015).
16. Khorasaninejad, M. & Capasso, F. Metalenses: versatile multifunctional photonic components. *Science* **358**, eaam8100 (2017).
17. Lin, D., Fan, P., Hasman, E. & Brongersma, M. L. Dielectric gradient metasurface optical elements. *Science* **345**, 298–302 (2014).
18. Vakil, A. & Engheta, N. Transformation optics using graphene. *Science* **332**, 1291–1294 (2011).
19. Berry, M. V. Quantal phase factors accompanying adiabatic. *Proc. R. Soc. A* **392**, 45–57 (1984).
20. Pancharatnam, S. Generalized theory of interference, and its application. *Proc. Ind. Acad. Sci. A* **44**, 247–262 (1956).
21. Bomzon, Z., Biener, G., Kleiner, V. & Hasman, E. Space-variant Pancharatnam–Berry phase optical elements with computer-generated subwavelength gratings. *Opt. Lett.* **27**, 1141–1143 (2002).
22. Bliokh, K. Y., Rodríguez-Fortuño, F. J., Nori, F. & Zayats, A. V. Spin-orbit interactions of light. *Nat. Photon.* **9**, 796–808 (2015).
23. Jungwirth, T., Wunderlich, J. & Olejník, K. Spin Hall effect devices. *Nat. Mater.* **11**, 382–390 (2012).
24. Le Sage, D. et al. Optical magnetic imaging of living cells. *Nature* **496**, 486–489 (2013).
25. Spitzer, F. et al. Routing the emission of a near-surface light source by a magnetic field. *Nat. Phys.* **14**, 1043–1048 (2018).
26. Rikken, G. L. J. A. & van Tiggelen, B. A. Observation of magnetically induced transverse diffusion of light. *Nature* **381**, 54–55 (1996).
27. Nagaosa, N. & Tokura, Y. Topological properties and dynamics of magnetic skyrmions. *Nat. Nanotechnol.* **8**, 899–911 (2013).
28. Onoda, M., Murakami, S. & Nagaosa, N. Hall effect of light. *Phys. Rev. Lett.* **93**, 083901 (2004).
29. Bliokh, K. Y., Smirnova, D. & Nori, F. Quantum spin Hall effect of light. *Science* **348**, 1448–1451 (2015).
30. Bliokh, K. Y., Niv, A., Kleiner, V. & Hasman, E. Geometrodynamics of spinning light. *Nat. Photon.* **2**, 748–753 (2008).
31. Yin, X., Ye, Z., Rho, J., Wang, Y. & Zhang, X. Photonic spin Hall effect at metasurfaces. *Science* **339**, 1405–1407 (2013).
32. Korger, J. et al. Observation of the geometric spin Hall effect of light. *Phys. Rev. Lett.* **112**, 113902 (2014).
33. Hosten, O. & Kwiat, P. Observation of the spin Hall effect of light via weak measurements. *Science* **319**, 787–790 (2008).
34. Bliokh, K. Y., Gorodetski, Y., Kleiner, V. & Hasman, E. Coriolis effect in optics: unified geometric phase and spin-Hall effect. *Phys. Rev. Lett.* **101**, 030404 (2008).
35. Zak, J. Geometric phase in magneto-optic Faraday rotation. *Phys. Lett. A* **154**, 471–474 (1991).
36. Aharonov, Y., Albert, D. Z. & Vaidman, L. How the result of a measurement of a component of the spin of a spin-1/2 particle can turn out to be 100. *Phys. Rev. Lett.* **60**, 1351–1354 (1988).
37. Temnov, V. V. et al. Active magneto-plasmonics in hybrid metal–ferromagnet structures. *Nat. Photon.* **4**, 107–111 (2010).
38. Sepúlveda, B., González-Díaz, J. B., García-Martín, A., Lechuga, L. M. & Armelles, G. Plasmon-induced magneto-optical activity in nanosized gold disks. *Phys. Rev. Lett.* **104**, 147401 (2010).
39. Belotelov, V. I. et al. Enhanced magneto-optical effects in magnetoplasmonic crystals. *Nat. Nanotechnol.* **6**, 370–376 (2011).
40. Guimarães, A. P. *Principles of Nanomagnetism* (Springer, 2009).
41. Lee, M., Callard, S., Seassal, C. & Jeon, H. Taming of random lasers. *Nat. Photon.* **13**, 445–448 (2019).
42. Berry, M. V. & Popescu, S. Evolution of quantum superoscillations and optical superresolution without evanescent waves. *J. Phys. A Math. Gen.* **39**, 6965–6977 (2006).
43. Rogers, E. T. F. et al. A super-oscillatory lens optical microscope for subwavelength imaging. *Nat. Mater.* **11**, 432–435 (2012).
44. Burch, K. S., Mandrus, D. & Park, J. G. Magnetism in two-dimensional van der Waals materials. *Nature* **563**, 47–52 (2018).
45. Gong, C. & Zhang, X. Two-dimensional magnetic crystals and emergent heterostructure devices. *Science* **363**, eaav4450 (2019).
46. Wang, R. F. et al. Artificial 'spin ice' in a geometrically frustrated lattice of nanoscale ferromagnetic islands. *Nature* **439**, 303–306 (2006).
47. Gilbert, I. et al. Emergent reduced dimensionality by vertex frustration in artificial spin ice. *Nat. Phys.* **12**, 162–165 (2016).
48. Canals, B. et al. Fragmentation of magnetism in artificial kagome dipolar spin ice. *Nat. Commun.* **7**, 11446 (2016).
49. Östman, E. et al. Interaction modifiers in artificial spin ices. *Nat. Phys.* **14**, 375–379 (2018).
50. Riek, C. et al. Direct sampling of electric-field vacuum fluctuations. *Science* **350**, 420–423 (2015).

Methods

Fabrication of ferromagnetic disordered metasurfaces. A fused silica substrate was cleaned by ultrasound in acetone and isopropanol, followed by a hot piranha solution and oxygen plasma. The positive e-beam resist with a thickness of approximately 500 nm was laid using the spinner at 3,000 r.p.m. in three consecutive layers of poly(methylmethacrylate) (PMMA): 495 A4, 495 A4 and 950 A3, which were baked in an oven at 180 °C for 15 min, 15 min and 35 min, respectively. A conductive thin chromium film of 15 nm was then deposited above the resist. The patterns of the nanostructures were transferred onto the resist using the Raith EBPG 5200 e-beam lithography system at 100 kV, and the discharging chromium layer was removed using Cr etchant CR-7. The PMMA mask obtained after development by a methyl isobutyl ketone (MIBK)/isopropanol (1:3) solution for 90 s was then used for the deposition of a thin nickel film of 150 nm in the Evatech vacuum evaporation system. The titanium layer of 15 nm was used for adhesion. The final nanopatterns were achieved by lift-off in acetone.

Experimental characterization of the PSHE. The PSHE generated from the nanoscale fluctuation of the ferromagnetic meta-atoms was measured by conducting the weak measurement while applying an electric-controlled magnetic field to magnetize the metasurface in the out-of-plane direction, as depicted in Fig. 3a. For a single measurement, we conducted the weak measurement three times, each time with a different external magnetic field, namely, $B=0$ and $B=\pm100$ mT. The reflected beam in the momentum space was captured by a CCD camera. The centroids of beams were calculated by integrating the intensity of the image in a region covering the entire diffraction-limited spot. The orientation of post-polarizer is precisely controlled by an electric-controlled rotator (Newport motion controller, ESP301) with a precision of 0.01 deg. By comparing the experimental results from different magnetic fields, the background effect can be eliminated, and the spin shift arising from the nanoscale fluctuation of the meta-atoms can be obtained.

Simulation and calculations of the space-variant magneto-optical effects from disordered ferromagnetic metasurfaces. To calculate the magneto-optical responses for a lattice of nickel nanoantennas, we conducted the simulations using the finite-difference time-domain (FDTD) method. A circular nickel nanoantenna with a radius R sits on the silica substrate, and periodic boundary conditions are applied on the sides. The dielectric tensor of the nickel is

$$\begin{bmatrix} \varepsilon & -i\varepsilon QM & 0 \\ i\varepsilon QM & \varepsilon & 0 \\ 0 & 0 & \varepsilon \end{bmatrix},$$

with Q the magneto-optical parameter and M the normalized magnetization, which ranges from -1 to 1, corresponding to different external magnetic fields. By changing the radius R and keeping a constant magnetization, for example $M=1$, we will obtain the magneto-optical response of the nickel nanoantenna as a function of R. Furthermore, we sample the nanoantennas in a lattice with random radii, composing a disordered metasurface with spatial fluctuation of the meta-atoms (nanoantennas). The near field of the metasurface for different magnetizations is calculated using the Huygens principle; the momentum space is calculated using Fourier transformation. Note that these calculations can also be applied for other materials (such as diamagnetic or paramagnetic materials) by replacing ε and Q. Therefore, the PSHE arising from disordered metasurfaces of different materials can be estimated.

Statistical analysis of the stochastic PSHE. The stochastic behaviour of the PSHE is theoretically studied by realizing a large number of disordered metasurfaces, each with a different realization of the random functions $f(x,y)$. Experimentally, this is achieved by fabricating a metasurface with a large area. We conducted the weak measurement with a relatively smaller beam many times, each time illuminating the metasurface in a different location.

Data availability

The data for Figs. 2–4 are available as source data. Other data that support the conclusions of this study are available from the corresponding author upon reasonable request.

Acknowledgements

We gratefully acknowledge financial support from the Israel Science Foundation (ISF); the US Air Force Office of Scientific Research (FA9550-18-1-0208) through their programme on Photonic Metamaterials; the Israel Ministry of Science, Technology and Space; the United States–Israel Binational Science Foundation (BSF); and, in part, the Technion via an Aly Kaufman Fellowship. The fabrication was performed at the Micro-Nano Fabrication & Printing Unit (MNF&PU), Technion.

Author contributions

All the authors contributed substantially to this work.

Competing interests

The authors declare no competing interests.

Additional information

Supplementary information is available for this paper at https://doi.org/10.1038/s41565-020-0670-0.

Correspondence and requests for materials should be addressed to E.H.

Peer review information *Nature Nanotechnology* thanks Vassilios Kapaklis, Francisco Rodríguez-Fortuño and the other, anonymous, reviewers for their contribution to the peer review of this work.